Elastic properties of the pyrite-type FeOOH–AlOOH system from first principles calculations

Elizabeth C. Thompson, Andrew J. Campbell, Jun Tsuchiya

[1]Department of Earth and Environmental Systems, Sewanee: The University of the South
[2]Department of the Geophysical Sciences, University of Chicago
[3]Geodynamics Research Center, Ehime University

Key Points:

- The elasticity, moduli, and seismic velocities of pyrite-type FeO_2H and AlO_2H were calculated from 60 to 140 GPa.
- Al-dominant $CaCl_2$-type (Al,Fe)OOH could coexist with Fe-rich pyrite-type (Al,Fe)O_2H in the Earth's lower mantle.
- Fe-rich pyrite-type (Al,Fe)O_2H may contribute to the reduced compressional and shear velocities of ULVZs.

Corresponding author: Elizabeth C. Thompson, ecthomps@sewanee.edu

Abstract

The stability, structure, and elastic properties of pyrite-type (FeS_2 structured) FeO_2H were determined using density functional theory based computations with a self-consistent Coulombic self-interaction term (U_{eff}). The properties of pyrite-type FeO_2H are compared to that of pyrite-type AlO_2H with which it likely forms a solid solution at high temperature, as well as the respective lower pressure $CaCl_2$-type polymorphs of both endmembers: ϵ-FeOOH and δ-AlOOH. Due to substantial differences in the $CaCl_2$-type→pyrite-type structural transition pressures of these endmembers, the stabilities of the (Al,Fe)O_2H solid solution polymorphs are anticipated to be compositionally driven at lower mantle pressures. As the geophysical properties of (Al,Fe)OOH are structurally dependant, interpretations regarding the contribution of pyrite-type FeO_2H to seismically observed features must take into account the importance of this broad phase loop. With this in mind, Fe-rich pyrite-type (Al,Fe)OOH may coexist with Al-dominant $CaCl_2$-type δ-(Al,Fe)OOH in the deep Earth. Furthermore, pyrite-type ($Al_{0.5\text{-}0.6}$,$Fe_{0.5\text{-}0.4}$)O_2H can reproduce the reduced compressional and shear velocities characteristic of seismically observed Ultra Low Velocity Zones (ULVZs) in the Earth's lowermost mantle while Al-dominant but Fe-bearing $CaCl_2$-type δ-(Al,Fe)OOH may contribute to Large Low Shear Velocity Provinces (LLSPs).

Plain Language Summary

Hydrogen storage and cycling in the deep Earth may have important implications for the chemistry and dynamics of Earth's mantle. Studies suggest a likely carrier of hydrogen into the Earth's lower mantle is the solid solution formed by ϵ-FeOOH, δ-AlOOH, and phase H ($MgSiO_4H_2$). At extreme pressures, ϵ-FeOOH and δ-AlOOH are both expected to transform into a pyrite-type crystal structure. This study provides a detailed examination of the stability and geophysical properties of pyrite-type FeO_2H at the pressures relevant to the Earth's lower mantle and compares these properties to those of pyrite-type AlO_2H. Based on these results we find that Al-dominant $CaCl_2$-type (Al,Fe)OOH may coexist with Fe-dominant pyrite-type (Al,Fe)O_2H in the Earth's lower mantle. Additionally, Fe-rich pyrite-type (Al,Fe)O_2H may contribute to the reduced compressional and shear velocities of Ultra Low Velocity Zones.

1 Introduction

Hydrogen storage and cycling in the deep Earth have important implications on the chemistry and dynamics of Earth's mantle. Recent results suggest a likely carrier of hydrogen into the Earth's lower mantle is the solid solution formed by the isostructural series ϵ-FeOOH, δ-AlOOH, and phase H ($MgSiO_4H_2$) (Ohira et al., 2014; Nishi et al., 2017; Kawazoe et al., 2017). At higher pressure, $CaCl_2$-type δ-AlOOH is predicted to transform into a pyrite structure (Tsuchiya & Tsuchiya, 2011) consisting of an AlO_2 framework with symmetrically bonded interstitial hydrogen (Figure 1). An analogous, high-pressure phase transition from $CaCl_2$-type ϵ-FeOOH to pyrite-type FeO_2H was discovered by high pressure experimentalists in the past few years, but the stoichometry and properties of this phase remain contested (Hu et al., 2016, 2017; Nishi et al., 2017; Liu et al., 2017; L. Yuan et al., 2018). The role of (Al,Fe)OOH in the hydrogen cycle of the deep Earth is likely significant, as unlike the other so-called 'alphabet' phases, high pressure structures of FeOOH and AlOOH, and intermediate compositions in the AlOOH-FeOOH-$MgSiO_4H_2$ system have been experimentally confirmed to be stable at average mantle geotherm pressure–temperature (P–T) conditions (Nishi et al., 2017; Duan et al., 2018; H. Yuan et al., 2019).

This study provides a detailed examination of the stability, structure, and geophysical properties of pyrite-type FeO_2H at pressure conditions relevant to the Earth's lower mantle. Importantly, these density function theory (DFT) calculations make use of a self-

consistent Coulombic self-interaction term (U_{eff}), which enables more accurate prediction of the electronic behavior in 3d transition metals (Kulik et al., 2006). These findings are presented alongside those of pyrite-type AlO_2H, with which pyrite-type FeO_2H likely forms a solid solution. This is supposition is supported by the recent synthesis of pyrite-type $Fe_{0.75}Al_{0.25}OOH$ at 160 GP by Nishi et al. (2020) and the experimentally confirmed solid solution of $CaCl_2$-type δ-(Al,Fe)OOH across a broad compositional range (Kawazoe et al., 2017; Nishi et al., 2019; Xu et al., 2019; Ohira et al., 2019; H. Yuan et al., 2019; Hsieh et al., 2019; Su et al., 2020). Importantly, aluminum substitution enhances the P–T stability of similar hydrous phases, including the lower-pressure $CaCl_2$-type polymorph of this system (Sano et al., 2008; Ohira et al., 2014; Pamato et al., 2015). Conversely, no pyrite-type polymorph of phase H ($MgSiO_4H_2$) has been reported, although pyrite-type magnesium peroxide (MgO_2) may be stable at lower mantle P–T conditions (Lobanov et al., 2015).

The mineralogical and elastic properties of the Fe- and Al-endmembers of the pyrite-type (Al,Fe)O_2H solid solution can be used to constrain the behavior of intermediate compositions for comparison with seismic observations of the deep Earth. In particular, a recent study suggested that partially dehydrated pyrite-type FeO_2H_X may contribute to the velocity reductions characteristic of Ultra Low Velocity Zones (ULVZs) near the core–mantle boundary (Liu et al., 2017). ULVZs are characterized by compressive and shear wave velocity reductions of up to 10% and 30%, respectively, compared to surrounding mantle material, and have morphologies consistent with a compositional rather than purely thermal origin (McNamara, 2019). Additionally, ULVZs are typically clustered near Large Low Shear Velocity Provinces (LLSVPs), and are more numerous but smaller than LLSVPs—extending only 10 to 20 km above the Earth's core–mantle boundary. Due to the geophysical proximity of ULVZs and LLSVPs, and the proposal that $CaCl_2$-type (Al,Fe)OOH contributes to LLSVPs (Thompson et al., 2017), we re-evaluated the potential for pyrite-type (Al,Fe)O_2H to contribute to the velocity reductions characteristic of ULVZs based on the formation of a solid solution rather than partial dehydration.

2 Methods

Density functional theory-based calculations of pyrite-type FeO_2H were performed using Quantum ESPRESSO, applying a Perdew-Burke-Ernzerhof generalized gradient approximation (GGA) to the exchange-correlation functional (Perdew et al., 1996) and a single effective on-site Coulombic self-interaction term (U_{eff}) determined using an internally consistent method. The internally consistent U_{eff} values used in our study were previously reported in Nishi et al. (2017). A generalized gradient approximation is necessary to accurately describe weak hydrogen bonding (Tsuchiya et al., 2002; Umemoto & Wentzcovitch, 2005), and the determination of an appropriate U_{eff} value is important to accurately describing the electronic structure and stability of iron-bearing phases (Jang et al., 2017). Optimized structures were determined using damped variable cell shape molecular dynamics (R. Wentzcovitch, 1991) in Quantum ESPRESSO (Giannozzi et al., 2009). The effective interaction of core electrons was approximated with previously evaluated norm-conserving pseudopotentials (Troullier & Martins, 1991) with the exception of iron, for which an ultrasoft pseudopotential was used (Ichikawa et al., 2014), enabling direct comparison to previously reported calculations for the lower pressure polymorph ϵ-FeOOH (Thompson et al., 2017). Ultrasoft pseudopotential and plane wave basis set are used to describe electronic structures. In this case, the electronic configuration $3s^2 3p^6 3d^{6.5} 4s^1 4p^0$ is pseudized with a sufficiently small core radius of 2 a.u. using the Vanderbilt scheme (Vanderbilt, 1990). The irreducible Brillouin zone was sampled by a 4×4×4 Monkhorst–Pack mesh (Monkhorst & Pack, 1976) and electronic wave functions were expanded in plane-waves with an energy cutoff of 80 Ry. The effects of larger energy cut-offs and k-point sampling were found to be negligible.

We conducted spin-polarized calculations, assuming a ferromagnetic low-spin state for ferric iron (Fe^{3+}) oxyhydroxide (majority spin − minority spin = 4) of pyrite structure FeOOH (Z=4). Only low spin ferromagnetic pyrite-type FeOOH was considered, as the lower pressure polymorph ϵ-FeOOH (Figure 1a) undergoes a spin transition at ∼45 GPa (Gleason et al., 2013; Ohira et al., 2019; Thompson et al., 2020) and the higher-pressure pyrite phase which has the same Fe-coordination number (i.e, 6) is presumably also in the lower-spin state at the high pressures of this study (70-140 GPa). Additionally, the unit cell volumes of low-spin calculations are consistent with experimental unit cell volumes (e.g. Nishi et al., 2020). Complementary first principles calculations of related high-pressure phases of FeOOH were performed to enable the determination of high-pressure phase relations for this composition. The details of the low-spin ferromagnetic ϵ-FeOOH calculation have been previously reported (Thompson et al., 2017). Additional FeOOH polymorphs including α-PbO_2-type (*Pbcn*) FeO_2H, *Pbca* FeO_2H, low-spin antiferromagnetic ϵ-FeOOH, high-spin antiferromagnetic ϵ-FeOOH, and high-spin ferromagnetic ϵ-FeOOH were evaluated using a fixed on-site Coulombic self-interaction term of $U = 5.0$ eV, with irreducible Brillouin zones sampled by a 4×4×4 Monkhorst–Pack mesh and an energy cutoff of 80 Ry. Due to the large calculated energy differences between FeOOH polymorphs, these phases were ruled out as potentially stable in the pressure range explored, and more sensitive self-interaction U calculations were deemed unnecessary.

Density functional theory-based calculations of δ-AlOOH and pyrite-type AlO_2H were recalculated using the same norm-conserving pseudopotentials of oxygen and hydrogen as our FeO_2H calculations to enable direct comparison between the Al- and Fe endmembers of these phases. A projector augmented wave method (PAW) pseudopotential was used for the aluminum atoms. Consistent with previous calculations of pyrite-type AlO_2H (Tsuchiya & Tsuchiya, 2011) and our FeO_2H calculations, these calculations also employed a generalized gradient approximation, sampled the irreducible Brillouin zones with a 4×4×4 Monkhorst–Pack mesh, and used an energy cutoff of 80 Ry. Elastic constants were determined by applying strains of magnitude 0.01–0.001 depending on the linearity of stress-strain relations (Karki et al., 2001) to relaxed, static (0 K) structures.

3 Results

3.1 Stability

The high-pressure phase relations of ϵ-FeOOH and pyrite-type FeO_2H were determined on the basis of least enthalpy (Figure 2a). Three of the FeOOH polymorphs evaluated in this study are potentially stable at the pressures of Earth's lower mantle: low-spin ferromagnetic ϵ-FeOOH at moderate pressure and either cubic ($Pa\bar{3}$) (Figure 1b) or orthorhombic (*Pbca*) (Figure 3) pyrite-type FeO_2H at high pressure. This newly recognized metastable orthorhombic (*Pbca*, Z=4, space group No. 63) structure has not yet been observed experimentally. The ϵ-FeOOH → pyrite-type FeO_2H transition based on these calculations occurs at ∼65 GPa, in good agreement with experiments (Nishi et al., 2017). The other FeOOH polymorphs evaluated in this study were were found to have significantly higher enthalpies (>0.04 e.v./formula unit higher) in the pressure range explored (60-140 GPa) and are therefore not expected to be stable at these conditions (Thompson et al., 2017).

The phase relations of δ-AlOOH and pyrite-type AlO_2H were also reevaluated (Figure 2b) and the δ-AlOOH → pyrite-type AlO_2H transition is predicted to occur at ∼190 GPa, similar to the 170 GPa transition pressure reported previously (Tsuchiya & Tsuchiya, 2011). This study did not evaluate the recently reported *Pbca* (Z=8) structure of AlOOH (Figure 1d) which may have an pressure-stability intermediate to the $CaCl_2$ and pyrite structures (Verma et al., 2018; Nishi et al., 2020), as no analogous *Pbca* (Z=8) structure

has been experimentally observed in FeOOH or intermediate (Al,Fe)OOH compositions. Initial structures with the orthorhombic pyrite symmetry (Pbca, Z=4) which stabilized in FeOOH, instead relaxed into cubic ($Pa\bar{3}$) structures at all evaluated pressures in AlOOH, indicating that the metastable structure exists only in the iron endmember. The significant difference in the $CaCl_2$-type → pyrite transition pressures between AlOOH and FeOOH follows the precedent established at lower pressures, as the α-AlOOH → $CaCl_2$-type transition occurs at higher pressure (∼17 GPa) (Suzuki et al., 2000; Tsuchiya et al., 2002) than the α-FeOOH → $CaCl_2$-type transition (∼5 GPa) (Gleason et al., 2008; Otte et al., 2009).

The high-pressure phase relations of the FeO_2H system parallel those of the AlO_2H system; namely the phase stable at the Earth's surface, goethite (α-FeOOH, isomorphous with diaspore, α-AlOOH), transforms to ϵ-FeOOH (isomorphous with δ-AlOOH) at moderate pressure, and subsequently transforms to a pyrite structure at the pressures of the Earth's mid-lower mantle. Experimentally, coexisting pyrite-structured and $CaCl_2$-type FeOOH polymorphs have been observed across a broad (∼30 GPa) pressure range, likely due to the modest enthalpy difference between these structures at the pressures of the mid-mantle (Lu & Chen, 2018). Furthermore, the ϵ-FeOOH → pyrite-type FeO_2H transition occurs at significantly lower pressure than the δ-AlOOH → pyrite-type AlO_2H transition, likely due to the difference in effective radius between low-spin iron and aluminum in accordance with the homologous rule (Verma et al., 2018). This indicates that (Al,Fe)O_2H solid solutions transition to the pyrite structure at pressures ranging from 65 to 190 GPa (Figure 2), and the pressure of the phase transition is strongly compositionally dependent. Combined with the energetics of the FeOOH system, it is likely that two phases (pyrite- and $CaCl_2$-type) of (Al,Fe)OOH coexist at finite temperature in this pressure range, with the Al/Fe ratio being higher in the $CaCl_2$-type phase and lower in the pyrite-type phase. These findings suggest that pyrite structured (Al,Fe)O_2H compositions exist as a minor mantle phase capable of ushering iron and hydrogen to the core-mantle boundary.

As previously described, two pyrite-type structures of FeO_2H are potentially stable at high pressure. Of these two FeO_2H structures, the cubic structure ($Pa\bar{3}$, space group No. 205) has a slightly lower enthalpy up to 120 GPa and is therefore the stable structure at these pressures. Nevertheless, the enthalpy difference is slight, with an enthalpy crossover leading to the orthorhombic pyrite structure (*Pbca*, space group No. 63) exhibiting slightly lower enthalpy at pressures >130 GPa. At the elevated temperatures of the Earth's lower mantle however, spin polarization disordering likely occurs. As the orthorhombically distorted pyrite structure was only observed in conjunction with spin-ordering, high temperatures are expected to lead to the preferential stabilization of the cubic phase up to core-mantle boundary pressures, consistent with the experimental observation of the cubic structure at concurrent high-pressure, high-temperature conditions (Hu et al., 2016, 2017; Nishi et al., 2017). Additionally, the formation of (Al,Fe)O_2H solid solutions should reduce the relative stability of the orthorhombic structure, as its formation is predicated on spin ordering as discussed below.

3.2 Electronic Properties

Difference in the $Pa\bar{3}$ and *Pbca* structures of pyrite-type FeO_2H are dictated by the d-orbital configuration of the iron atoms in these phases, as shown in the spin-polarization density maps of Figure 3. Cubic ($Pa\bar{3}$) pyrite-type FeO_2H structures were optimized using a t_{2g} d-orbital configuration, while orthorhombic (*Pbca*) pyrite-type FeO_2H is the optimized structure resulting from any non-t_{2g} d-orbital occupation. In the case of the orthorhombic (*Pbca*) structure, the spin polarization isosurfaces are oriented such that they are in close proximity to the hydrogen atoms, creating strong repulsive forces and producing an orthorhombic Jahn-Teller distortion, with a distortion index (Baur, 1974) (DI) of ∼0.001. Conversely, in the cubic ($Pa\bar{3}$) structure, the spin polarization isosurfaces are

Table 1. Birch-Murnaghan equation of state parameters for the high-pressure pyrite structures of FeO_2H and AlO_2H based on self-consistent U-value calculations from 60 to 140 GPa. Values in parentheses are uncertainties on the last digit. These uncertainties are from an unweighted fit in which each point has zero measurement uncertainty.

		V_0 (Å^3)	K_0 (GPa)	K_0'
$Pa\bar{3}$ FeO_2H	This study	112.56(8)	240(1)	4 (fixed)
$Pa\bar{3}$ FeO_2H	This study	113.88(8)	213(1)	4.33(2)
$Pa\bar{3}$ FeO_2H	Huang et al. (2019)	112.32	211.3	4.44
$Pa\bar{3}$ AlO_2H	This study	109.89(4)	214.16(4)	4 (fixed)
$Pa\bar{3}$ AlO_2H	This study	109.88(2)	214.4(4)	3.997(4)

oriented antithetical to both hydrogen and iron atoms, with minimal distortion (DI ∼0.00001). Additionally, in both structures the densities of state at all explored pressures (60-140 GPa) exhibit nonzero bandgaps indicative of insulator behavior (Figure S1). This differs from the reported electronic properties of FeO_2 (Jang et al., 2017), in that neither pyrite-type FeO_2H undergoes a metal-insulator transition in the pressure range relevant to the Earth's mantle. Although pyrite-type FeO_2 is unlikely stable at the redox conditions of the deep Earth, the difference in the electronic properties of pyrite-type FeO_2 and pyrite-type FeO_2H introduces some uncertainty into the electronic properties of pyrite-type FeO_2H_X, which warrants future study.

3.3 Structure and Equation of State

Lattice parameters of the optimized structures of *Pbca* FeO_2H, $Pa\bar{3}$ FeO_2H, and $Pa\bar{3}$ AlO_2H are reported in Table S1. Equation of state parameters for $Pa\bar{3}$ pyrite-type FeO_2H and AlO_2H were determined by fitting the volume of optimized structures of GGA+U calculations between 60 and 140 GPa to third-order Birch-Murnaghan equations of state (Birch, 1947):

$$P(V) = \frac{3\kappa_0}{2}\left[\left(\frac{V_0}{V}\right)^{\frac{7}{3}} - \left(\frac{V_0}{V}\right)^{\frac{5}{3}}\right]\left\{1 + \frac{3}{4}\left(\kappa_0' - 4\right)\left[\left(\frac{V_0}{V}\right)^{\frac{2}{3}} - 1\right]\right\} \quad (1)$$

in which κ_0 is the bulk modulus at ambient pressure, κ_0' is the first pressure derivative of the bulk modulus, and V_0 is the volume per formula unit at ambient pressure. Equation of state parameters from these fits are presented in Table 1, and include parameterizations in which κ_0' was treated as either a fixed ($\kappa_0' = 4$) or free parameter. The iron endmember, FeO_2H, has a larger volume than AlO_2H, and is also less compressible; hence the relative volume difference between these two structures increases with pressure from 1.3% at 60 GPa to 1.6% at 140 GPa (Figure 4a).

Neither pyrite-type FeO_2H nor AlO_2H contain discreet hydroxyl units, and unlike their respective lower pressure polymorphs do not undergo pressure-induced hydrogen bond symmetrization, as the hydrogen bonds are symmetric even at the lowest pressures of these phases' respective stabilities (Figure 4b). Additionally, as both iron and aluminum endmembers contain only symmetric bonds across their stability ranges, solid solutions from these systems are more likely to behave in a manner consistent with a linear mixing model than in systems where pressure-induced hydrogen bond symmetrization is a concern (Panero & Caracas, 2009).

Table 2. Comparison of the elastic properties of pyrite-type FeO_2H and AlO_2H as a function of pressure (P) from 60 to 140 GPa. Densities (ρ) are in units of g/cm^3, and bulk (κ) and shear (μ) moduli are in GPa.

P	*Pbca* FeO_2H			$Pa\bar{3}$ FeO_2H			$Pa\bar{3}$ AlO_2H		
	ρ	κ	μ	ρ	κ	μ	ρ	κ	μ
60	—	—	—	6.248	449.0	174.0	4.389	435.0	228.9
70	6.401	481.0	134.1	6.383	485.9	179.5	4.488	469.5	237.9
80	6.530	517.1	161.5	6.510	524.8	184.7	4.581	503.8	247.5
90	6.652	552.8	170.1	6.630	560.8	187.4	4.670	536.8	256.8
100	6.769	590.5	183.3	6.746	597.3	189.5	4.755	569.7	265.8
110	6.880	626.1	188.4	6.856	632.8	191.2	4.837	602.9	274.3
120	6.988	661.5	194.5	6.962	667.4	192.6	4.916	635.4	282.7
130	7.091	696.5	200.8	7.064	702.9	194.5	4.992	668.3	290.4
140	7.190	731.3	207.0	7.162	737.5	194.4	5.065	700.6	298.2

3.4 Elastic Constants and Moduli

The elastic tensors of pyrite-type AlO_2H and both polymorphs of pyrite-type FeO_2H were determined up to the pressure of the core-mantle boundary (Figure 5, Table S2, Table S3) and the mechanical stability of all three structures were verified with the relevant stability criteria (Born & Huang, 1954; Karki et al., 1997). Fully describing the elasticity of an orthorhombic phase requires nine elastic constants, but for small distortions these can be averaged to produce a cubic-equivalent three constant tensor, enabling comparison between the orthorhombic (*Pbca*) and cubic ($Pa\bar{3}$) polymorphs of FeO_2H. Details of this averaging are given in Equations S1, S2, and S3 and the full elastic constant tensor of the orthorhombic (*Pbca*) structure are given in Table S3. As shown in Table S2, the elastic constants of $Pa\bar{3}$ and *Pbca* FeO_2H are in good agreement, differing by <5% at pressures greater than 100 GPa. However, the elastic constants of pyrite-type AlO_2H differ more significantly from those of FeO_2H, both in magnitude and to a lesser degree pressure dependence (Figure 5).

The bulk and shear moduli of pyrite-type FeO_2H and AlO_2H were calculated from single crystal elastic constants using the Voigt-Reuss-Hill averaging scheme (Hill, 1952) (Table 2). Bulk moduli of all three phases (*Pbca* FeO_2H, $Pa\bar{3}$ FeO_2H, and $Pa\bar{3}$ AlO_2H) are remarkably similar across the pressure range investigated, with <5% variation. The differences in shear moduli are considerably more substantial. Orthorhombic *Pbca* FeO_2H exhibits a reduced shear modulus compared to the cubic structure at pressures <100 GPa, due to differences between the C_{44} of cubic FeO_2H and the C_{44}, C_{55}, and C_{66} of orthorhombic FeO_2H. These differences diminish with increasing pressure, and at pressures >100 GPa both polymorphs of pyrite-type FeO_2H exhibit shear moduli within ~6% of one another. No such convergence occurs between the shear moduli of $Pa\bar{3}$ FeO_2H and AlO_2H. At 60 GPa the shear modulus of AlO_2H is ~32% greater than that of FeO_2H, and with increased pressure this divide widens, so that by core-mantle boundary (CMB) pressures the difference is ~53%.

3.5 Sound Velocities

Elastic moduli of $Pa\bar{3}$ pyrite-type FeO_2H and AlO_2H were used to calculate the aggregate sound velocities of both endmember compositions as a function of pressure (Figure 6), to facilitate comparison to seismologically observable properties of Earth's interior. Across the pressure range investigated, the compressional velocity (V_P) of the Al-

and Fe-endmembers differ by a nearly constant margin of 24-25%. Conversely, the shear velocities (V_S) of FeO_2H and AlO_2H differ not only in magnitude but pressure dependence, such that the V_S of pyrite-type AlO_2H is elevated ∼37-46% relative to that of pyrite-type FeO_2H, with the greatest disparity occurring at the pressures of the lowermost mantle. However, as the calculated δ-AlOOH → pyrite-type AlO_2H transition occurs at pressures exceeding those of the Earth's mantle (i.e., P >136 GPa), the elastic behaviors of the Al-endmember at these pressures are relevant only in that they allow us to constrain the moduli and sound velocities of intermediate (Al,Fe)O_2H compositions expected to be stable at the pressure of the lowermost mantle.

The elastic constants and sound velocities of pyrite-type FeO_2H from this study are presented alongside the static calculation results of Huang et al. (2019). The FeO_2H densities from these studies differ by less than 2% and the sound velocities of our study are in reasonable agreement with the V_P and V_S differing by 8-9% and 1-8%, respectively. However, the previously reported V_P and V_S pressure trends reported by Huang et al. (2019) exhibit slightly higher positive pressure dependencies than this study (Figure 6). These velocity differences can be attributed to the different input parameters of these studies including the use of fixed U and J values of the Huang et al. (2019) study versus the internally consistent U_{eff} of this study.

In addition to aggregate sound velocities, the single crystal polarization anisotropy (AV_S) of $Pa\bar{3}$ pyrite-type FeO_2H and AlO_2H were determined using Equation S4 as shown in Figure 7. The maximum polarization anisotropy of pyrite-type FeO_2H and AlO_2H are compared to the lower pressure polymorphs ϵ-FeOOH and δ-AlOOH (Figure 8). In both endmembers the maximum polarization anisotropy is greatest along the {110} and lowest along the {100} and {111}. Our pyrite-type FeO_2H results are consistent with, although slightly lower than, the maximum anisotropies published by Huang et al. (2019) at comparable pressures. Both ϵ-FeOOH and δ-AlOOH exhibit a strong degree of polarization anisotropy —a property that increases with increasing pressure (Tsuchiya & Mookherjee, 2015; Thompson et al., 2017). However, the polarization anisotropy of pyrite-type FeO_2H and AlO_2H is significantly lower than their respective $CaCl_2$-type counterparts. Based on these constraints, for a fixed (Al,Fe)OOH composition the polarization anisotropy of the pyrite-type polymorph is expected to be less than that of a δ-(Al,Fe)OOH polymorph of the same composition at the same pressure.

4 Discussion

Based on our calculations, the transition pressure of $CaCl_2$-type (Al,Fe)OOH solid solutions, to the pyrite structure is strongly compositionally dependent and both $CaCl_2$-type and pyrite-type (Al,Fe)OOH may persist up to core-mantle boundary pressures. The $CaCl_2$ structure is expected to be stabilized by the incorporation of aluminum, while compositions predominated by iron likely transform to the pyrite structure at the pressures of the lowermost mantle. These results are consistent with experimental work by L. Yuan et al. (2018), whose evaluation of the MgO–Al_2O_3–Fe_2O_3–SiO_2–H_2O at the P–T conditions of the lowermost mantle resulted in phase assemblages containing coexisting aluminum-dominant $CaCl_2$-type AlOOH–FeOOH–$MgSiO_2(OH)_2$ (δ-phase), pyrite-type FeO_2H, bridgmanite, and post-perovskite.

Due to the likely coexistence Al-dominant δ-(Al,Fe)OOH and Fe-dominant pyrite-type (Al,Fe)O_2H at the conditions of Earth's mantle, it is necessary to compare and contrast the geophysical properties of the endmember polymorphs to develop constraints for comparison to seismic observations. The seismic signature of the Al-endmember is not expected to change dramatically across the $CaCl_2$-type→pyrite-type phase transition, as both the compressional and shear wave velocities of δ-AlOOH and pyrite-type AlO_2H differ by <2%. However, while the compressional velocities of pyrite-type FeO_2H

and ϵ-FeOOH differ by only 2-4%, the difference in shear velocity is more substantial, with the V_S of ϵ-FeOOH reduced 11-16% relative to pyrite-type FeO_2H.

A recent study by Liu et al. (2017) concluded that Ultra Low Velocity Zones (ULVZs) might be reasonably explained by domains at the core-mantle boundary rich in pyrite-type FeO_2H_X—a partially dehydrated form of stoichiometric FeO_2H. Although it is not resolved whether the persistence of deep Earth structures dominated by hydrous phases at geological timescales may be mitigated by the rate of hydrogen diffusion in the Earth's mantle (Mackwell & Kohlstedt, 1990; Novella et al., 2017), it is important to evaluate this in the context of the likely solid solution properties of these phases. We re-evaluated the potential for pyrite-type FeO_2H and the solid solution it likely forms with AlO_2H to contribute to the seismic velocity reductions characteristic of ULVZs (McNamara, 2019). Sound velocities of intermediate (Al,Fe)O_2H compositions were linearly interpolated from the velocities of the endmember compositions, and bridgmanite ($MgSiO_3$-perovskite), as the most abundant mineral of the lower mantle, was used as a proxy for the bulk lower mantle. This allowed for the direct comparison of the static calculations of the velocities of bridgmanite (R. M. Wentzcovitch et al., 2004) against those of (Al,Fe)OOH, in the absence of additional thermoelastic calculations. Although increasing attention has been paid recently to how non-ideality of solid solutions affect their elastic properties (e.g., Myhill, 2018), the similar chemistry, structure, and unit cell volumes of the Fe- and Al-endmembers suggest that non-ideality in the high-pressure (Al,Fe)OOH system is minimal. For example, experimentally determined unit cell volumes of $CaCl_2$-type (Al,Fe)OOH trend linearly with measured Fe/(Fe+Al) ratios at ambient (i.e., fixed) pressure and temperature. The non-ideality of pyrite-type (Al,Fe)O_2H, for which there is limited experimental data, is expected to be comparable to that of the $CaCl_2$-type (Al,Fe)OOH, as the chemical and structural similarities are preserved and the calculated volume difference of the Fe- and Al-endmembers is reduced in the higher pressure pyrite structure. Based on these calculations, we determined that pyrite-structured $(Al_X,Fe_{1\text{-}X})O_2H$ with X =0.5-0.6 can simultaneously match the 10% V_P and 30% V_S reductions relative to the bulk mantle (i.e., bridgmanite) characteristic of these regions. Solid solutions in this compositional range are 6-8% denser than bridgmanite, providing gravitational stability at the core mantle boundary, although this density contrast may be reduced at the high temperatures of the mantle and by thermochemical convection. Importantly, this shows that iron-rich pyrite-type solid solution enriched regions may contribute to observed ULVZs without invoking dehydration.

Al-rich $CaCl_2$-type (Al,Fe)OOH solid solutions, referred to as δ-(Al,Fe)OOH, may contribute to the reduced shear wave velocities characteristic of large low shear velocity provinces (LLSVPs) (Thompson et al., 2017; Su et al., 2020). Physically proximal and compositionally similar, LLSVPs containing δ-(Al,Fe)OOH and ULVZs containing pyrite-type (Al,Fe)O_2H may share a geochemical origin. As gravitationally unstable δ-(Al,Fe)OOH sinks to the core-mantle boundary, elevated temperatures and reaction with core material may produce elevated levels of iron enrichment, driving the transition to the pyrite structure. Additionally, pyrite-type FeO_2H or FeO_2H_X may be produced by the reaction of hydrous phases with iron at the core-mantle boundary (L. Yuan et al., 2018). Since non-stoichiometric pyrite-type FeO_2H_X may develop at the core-mantle boundary, the electronic properties as a function of hydrogen content should be experimentally investigated. Due to the difference in electronic behavior of FeO_2 and FeO_2H, the incorporation or loss of hydrogen could affect the electromagnetic interaction between the liquid core and lower mantle, as hydrogen seems to promote insulator behavior and might inhibit this coupling.

Lastly, there is sharp contrast in the maximum shear wave polarization anisotropy of pyrite-type FeO_2H and AlO_2H compared to their respective lower pressure polymorphs—a contrast which is greatest at the pressures of the lowermost mantle (Figure 8). As such, the $CaCl_2$-type $\rightarrow$ pyrite-type structural transition in (Al,Fe)OOH may be marked by

an observable seismic signature. The sharpness of such a signal would depend on two primary factors: (1) the width of the phase loop, as the iron and aluminum endmembers have phase boundaries >100 GPa apart, and (2) the degree of lattice preferred orientation (LPO) locally in each phase. Interpolating from the stability of the Al- and Fe-endmembers, pyrite-type $(Al_X,Fe_{1-X})O_2H$ with X<0.6 is likely stable at CMB pressures, where it would exhibit low to negligible degrees of shear wave polarization. Conversely, $CaCl_2$-type $(Al_X,Fe_{1-X})OOH$ in which X>0.6 may also be stable at CMB pressures, and would be characterized by strongly horizontally polarized shear waves consistent with observations of horizontally polarized shear waves at the base of the mantle (Thompson et al., 2017).

5 Conclusion

We have presented a computational analysis of the stability, structure, and elastic properties of high-pressure pyrite-type FeO_2H. The structure, transition pressure, and equation of state of this phase was compared to that of pyrite-type AlO_2H, with which it likely forms a solid solution. Based on our first principles calculations, the stable structure of pyrite-type FeO_2H is cubic, although at sufficiently high pressure a Jahn-Teller distortion in FeO_2H may produce an orthorhombic structure with pressure-dependent, non-fixed lattice parameter ratios. Within the Earth's interior however, the $Pa\bar{3}$ structure is expected to dominate, as at mantle temperature conditions the Jahn-teller distortions responsible for producing the *Pbca* symmetry are presumably randomly oriented within FeOOH crystal.

$CaCl_2$-structured $(Al,Fe)O_2H$ solid solutions transform to the pyrite structure between 65 and 190 GPa and the transition pressure is strongly compositionally dependent. Owing to this compositionally driven phase boundary, it is likely that Al-dominant $CaCl_2$-type $(Al,Fe)O_2H$ coexists with Fe-rich pyrite-type $(Al,Fe)O_2H$ in the Earth's lower mantle. Both $CaCl_2$-type (Al,Fe)OOH and pyrite-type $(Al,Fe)O_2H$ solid solutions may deliver hydrogen through the Earth's lower mantle to the core-mantle boundary, but the seismic properties of these solid solutions are strongly tied to their structure. Al-dominant compositions are likely stable to CMB pressures in the $CaCl_2$ structure and may help explain the shear wave velocity reductions of LLSVPs. Conversely, Fe-rich compositions will transform to the pyrite-structure at lower mantle pressures and may contribute to the reduced compressional and shear velocities observed in ULVZs. Hence, it is important that when connecting mineral physics results to seismic observations, one takes into account the composition, structure, and stability of the solid solution rather than an isolated endmember composition. Future experimental work probing the proposed phase loop and exploring the non-ideality of the (Al,Fe)OOH system at the conditions of the Earth's lower mantle would refine our understanding of pyrite-type (Al,Fe)OOH as a major agent of hydrogen transportation in the deep Earth and as a potential contributor to ULVZs.

Acknowledgments

The authors declare no real or perceived financial conflicts of interest related to this work. Supporting information can be found in the supplemental documents and the data is also hosted in the Open Science Framework (OSF) at doi:10.17605/OSF.IO/EBY4J. This work was supported by a National Science Foundation Postdoctoral Fellowship under grant EAR-1725673 and EAPSI Program grant SP-1612833, jointly funded through the U.S. National Science Foundation and the Japan Society for the Promotion of Science (JSPS) for E.T. This study was supported in part by NSF grant EAR-1651017 for A.C. This study was also partly supported by JSPS KAKENHI grants JP26400516, JP26287137, and JP15H05834 for J.T.

References

Baur, W. (1974). The geometry of polyhedral distortions. predictive relationships for the phosphate group. *Acta Crystallogr. B.*, *30*, 1195–1215. doi: 10.1107/S0567740874004560

Birch, F. (1947). Finite elastic strain of cubic crystals. *Phys. Rev.*, *71*, 809.

Born, M., & Huang, K. (1954). *Dynamical theory of crystal lattices.* London, UK: Oxford University Press.

Duan, Y., Sun, N., Wang, S., Li, X., Guo, X., Ni, H., ... Mao, Z. (2018). Phase stability and thermal equation of state of δ-AlOOH: Implication for water transportation to the Deep Lower Mantle. *Earth and Planetary Science Letters*, *494*, 92–98. doi: 10.1016/j.epsl.2018.05.003

Giannozzi, P., Baroni, S., Bonini, N., Calandra, M., Car, R., Cavazzoni, C., ... Wentzcovitch, R. (2009). Quantum espresso: A modular and open-source software project for quantum simulations of materials. *J. Phys. Condens. Matter*, *21*, 395502.

Gleason, A., Jeanloz, R., & Kunz, M. (2008). Pressure-temperature stability studies of FeOOH using X-ray diffraction. *American Mineralogist*, *11–12*, 1882–1885. doi: 10.2138/am.2008.2942

Gleason, A., Quiroga, C., Suzuki, A., Pentcheva, R., & Mao, W. (2013). Symmetrization driven spin transition in ϵ-FeOOH at high pressure. *Earth and Planetary Letters*, *379*, 49–55. doi: 10.1016/j.epsl.2013.08.012

Hill, R. (1952). The elastic behavior of a crystalline aggregate. *Proc. Phys. Soc.*, *65*, 349–354.

Hsieh, W.-P., Ishii, T., Chao, K.-H., Tsuchiya, J., Deschamps, F., & Ohtani, E. (2019). Spin transition of iron in δ-AlOOH induces thermal anomalies in earth's lower mantle. *Geophysical Research Letters*, *47*, e2020GL087036. doi: 10.1029/2020GL087036

Hu, Q., Kim, D., Liu, J., Meng, Y., & Mao, H.-K. (2016). FeO_2 and FeOOH under deep lower-mantle conditions and Earth's oxygen-hydrogen cycles. *Nature*, *534*, 241–245.

Hu, Q., Kim, D., Liu, J., Meng, Y., Yang, L., Zhang, D., ... Mao, H.-K. (2017). Dehydrogenation of goethite in Earth's deep lower mantle. *Proc. Natl. Acad. Sci.*, *114*, 1498–1501.

Huang, S., Qin, S., & Wu, X. (2019). Elasticity and anisotropy of the pyrite-type FeO_2H-FeO_2 system in Earth's lowermost mantle. *Journal of Earth Science*, *30*, 1293–1301. doi: 10.1007/s12583-018-0836-y

Ichikawa, I., Tsuchiya, T., & Tange, Y. (2014). The *P-V-T* equation of state and thermodynamic properties of liquid iron. *J. Geophys. Res*, *119*, 240–2525.

Jang, B., Kim, D., & Shim, J. (2017). Metal-insulator transition and the role of electron correlation in FeO_2. *Phys. Rev. B*, *95*, 075144.

Karki, B., Ackland, G., & Crain, J. (1997). Elastic instabilities in crystals from ab initio stress-strain relations. *Journal of Physics: Condensed Matter*, *41*, 8579–8589. doi: 10.1088/0953-8984/9/41/005

Karki, B., Stixrude, L., & Wentzcovitch, R. (2001). High-pressure elastic properties of major materials of earth's mantle from first principles. *Reviews of Geophysics*, *39*, 507–534. doi: 10.1029/2000RG000088

Kawazoe, T., Ohira, I., Ishii, T., Ballaran, T. B., Mccammon, C., Suzuki, A., & Ohtani, E. (2017). Single crystal synthesis of δ-(Al,Fe)OOH. *American Mineralogist*, *102*, 1953–1956.

Kulik, H., Cococcioni, M., Sherli, D., & Marzari, N. (2006). Density functional theory in transition-metal chemistry: A self-consistent Hubbard U approach. *Phys. Rev. Lett.*, *97*, 103001.

Liu, J., Hu, Q., Kim, D., Wu, Z., Wang, W., Xiao, Y., ... Mao, W. (2017). Hydrogen-bearing iron peroxide and the origin of ultralow-velocity zones. *Nature*, *551*, 494–497.

Lobanov, S., Zhu, Q., Holtgrewe, N., Prescher, C., Prakapenka, V., Oganov, A., & Goncharov, A. (2015). Stable magnesium peroxide at high pressure. *Sci. Rep.*, *97*, 13582.

Lu, C., & Chen, C. (2018). High-pressure evolution of crystal bonding structures and properties of FeOOH. *J. Phys. Chem. Lett.*, *9*(9), 2181–2185. doi: 10.1021/acs.jpclett.8b00947

Mackwell, S., & Kohlstedt, D. (1990). Diffusion of hydrogen in olivine: Implications for water in the mantle. *J. Geophys. Res.*, *95*, 5079–5088.

Mainprice, D., Hielscher, R., & Schaeben, H. (2011). Calculating anisotropic physical properties from texture data using the MTEX open-source package. *Geol. Soc. London Spec. Publ.*, *360*, 175–192.

McNamara, A. (2019). A review of large low shear velocity provinces and ultra low velocity zones. *Tectonophysics*, *760*, 199–220. doi: 10.1016/j.tecto.2018.04.015

Momma, K., & Izumi, F. (2008). Vesta: A three-dimensional visualization system for electronic and structural analysis. *J. Appl. Crystallogr.*, *41*, 653–658.

Monkhorst, H., & Pack, J. (1976). Special points for brillouin-zone integrations. *Phys. Rev. B*, *13*, 5188–5192.

Myhill, R. (2018). The elastic solid solution model for minerals at high pressures and temperatures. *Contributions to Mineralogy and Petrology*, *173*. doi: 10.1007/s00410-017-1436-z

Nishi, M., Kuwayama, Y., & Tsuchiya, J. (2020). New aluminum hydroxide at multimegabar pressures: Implications for water reservoirs in deep planetary interiors. *Icarus*. doi: 10.1016/j.icarus.2019.113539

Nishi, M., Kuwayama, Y., Tsuchiya, J., & Tsuchiya, T. (2017). The pyrite-type high-pressure form of FeOOH. *Nature*, *547*, 205–208.

Nishi, M., Tsuchiya1, J., Kuwayama, Y., Arimoto1, T., Tange, Y., Higo, Y., ... Irifune, T. (2019). Solid solution and compression behavior of hydroxides in the lower mantle. *Journal of Geophysical Research: Solid Earth*, *124*, 10231–10239. doi: 10.1029/2019JB018146

Novella, D., Jacobsen, B., Weber, P., Tyburczy, J., Ryerson, F., & Frane, W. D. (2017). Hydrogen self-diffusion in single crystal olivine and electrical conductivity of the Earth's mantle. *Sci. Rep.*, *7*, 5344.

Ohira, I., Jackson, J., Solomatova, N., Sturhahn, W., Finkelstein, G., Kamada, S., ... Ohtani, E. (2019). Compressional behavior and spin state of δ(Al,Fe)OOH at high pressures. *American Mineralogist*, *104*, 1273–1284. doi: 10.2138/am-2019-6913

Ohira, I., Ohtani, E., Sakai, T., Miyahara, M., Hirao, N., Ohishi, Y., & Nishijima, M. (2014). Stability of a hydrous δ-phase, AlOOH-$MgSiO_2(OH)_2$, and a mechanism for water transport into the base of the lower mantle. *Earth Planet. Sci. Lett.*, *401*, 12–17.

Otte, K., Pentcheva, R., Schmahl, W., & Rustad, J. (2009). Pressure-induced structural and electronic transitions in FeOOH from first principles. *Physical Review B*, *80*, 205116. doi: 10.1103/PhysRevB.80.205116

Pamato, M., Myhill, R., Ballaran, T. B., Frost, D., Heidelbach, F., & Miyajima, N. (2015). Lower-mantle water reservoir implied by the extreme stability of a hydrous aluminosilicate. *Nat. Geo.*, *8*, 75–79.

Panero, W., & Caracas, R. (2009). Stability of phase h in the $MgSiO_4H_2$-AlOOH-SiO_2 system. *Earth Planet. Sci. Lett.*, *463*, 171–177.

Perdew, J. P., Burke, K., & Ernzerhof, M. (1996). Generalized gradient approximation made simple. *Phys. Rev. Lett.*, *77*, 3865–3868.

Sano, A., Ohtani, E., Kondo, T., Hirao, N., Sakai, T., Sata, N., ... Kikegawa, T. (2008). Aluminous hydrous mineral δ-AlOOH as a carrier of hydrogen into the core-mantle boundary. *Geophys. Res. Lett.*, *35*, L03303.

Su, X., Zhao, C., Lv, C., Zhuang, Y., Salke, N., Xu, L., ... Liu, J. (2020). The

effect of iron on the sound velocities of δ-AlOOH up to 135 gpa. *Geoscience Frontiers*. doi: 10.1016/j.gsf.2020.08.012

Suzuki, A., Ohtani, E., & Kamada, T. (2000). A new hydrous phase δ-AlOOH synthesized at 21 GPa and 1000 C. *Phys. Chem. Minerals*, *27*, 689–693.

Thompson, E., Campbell, A., & Tsuchiya, J. (2017). Elasticity of ϵ-FeOOH: Seismic implications for Earth's lower mantle. *J. Geophys. Res.*, *122*(7), 5038–5047.

Thompson, E., Davis, A., Brauser, N., Liu, Z., Prakapenka, V., & Campbell, A. (2020). Phase transitions in ϵ-FeOOH at high pressure and ambient temperature. *American Mineralogist*, *105*, 1769–1777. doi: 10.2138/am-2020-7468

Troullier, N., & Martins, J. (1991). Efficient pseudopotentials for planewave calculations. *Phys. Rev. B*, *43*, 1993–2006.

Tsuchiya, J., & Mookherjee, M. (2015). Crystal structure, equation of state, and elasticity of phase H ($MgSiO_4H_2$) at Earth's lower mantle pressures. *Sci. Rep.*, *5*, 15534.

Tsuchiya, J., & Tsuchiya, T. (2011). First principles prediction of a high-pressure hydrous phase of AlOOH. *Phys. Rev. B*, *83*, 054115.

Tsuchiya, J., Tsuchiya, T., Tsuneyuki, S., & Yamanaka, T. (2002). First principles calculation of a high-pressure hydrous phase δ-AlOOH. *Geophys. Res. Lett.*, *19*, 1909.

Umemoto, K., & Wentzcovitch, R. (2005). Theoretical study of the isostructural transformation in ice VIII. *Phys. Rev. B*, *71*, 012102.

Vanderbilt, D. (1990). Soft self-consistent pseudopotentials in a generalized eigenvalue formalism. *Phys. Rev. B*, *41*, 7892–7895.

Verma, A. K., Modak, P., & Stixrude, L. (2018). New high-pressure phases in MOOH (M = Al, Ga, In). *American Mineralogist*, *103*, 1906–2018.

Wentzcovitch, R. (1991). Invariant molecular dynamics approach to structural phase transitions. *Phys. Rev. B*, *44*, 2358–2362.

Wentzcovitch, R. M., Karki, B. B., Cococcioni, M., & de Gironcoli, S. (2004). Thermoelastic properties of $MgSiO_3$-perovskite: Insights on the nature of the Earth's lower mantle. *Physical Review Letters*, *92*, 018501.

Xu, C., Nishi, M., & Inoue, T. (2019). Solubility behavior of δ-AlOOH and ϵ-FeOOH at high pressures. *American Mineralogist*, *104*, 1416–1420. doi: 10.2138/am-2019-7064

Yuan, H., Zhang, L., Ohtani, E., Meng, Y., Greenberg, E., & Prakapenka, V. (2019). Stability of fe-bearing hydrous phases and element partitioning in the system MgO-Al_2O_3-Fe_2O_3-SiO_2-H_2O in Earth's lowermost mantle. *Earth and Planetary Science Letters*, *524*, 115714. doi: 10.1016/j.epsl.2019.115714

Yuan, L., Ohtani, E., Ikuta, D., Kamada, S., Tsuchya, J., Naohisa, H., ... Suzuki, A. (2018). Chemical reactions between Fe and H_2O up to megabar pressures and implications for water storage in the Earth's mantle and core. *Geophys. Res. Lett.*, *45*, 1330–1338.

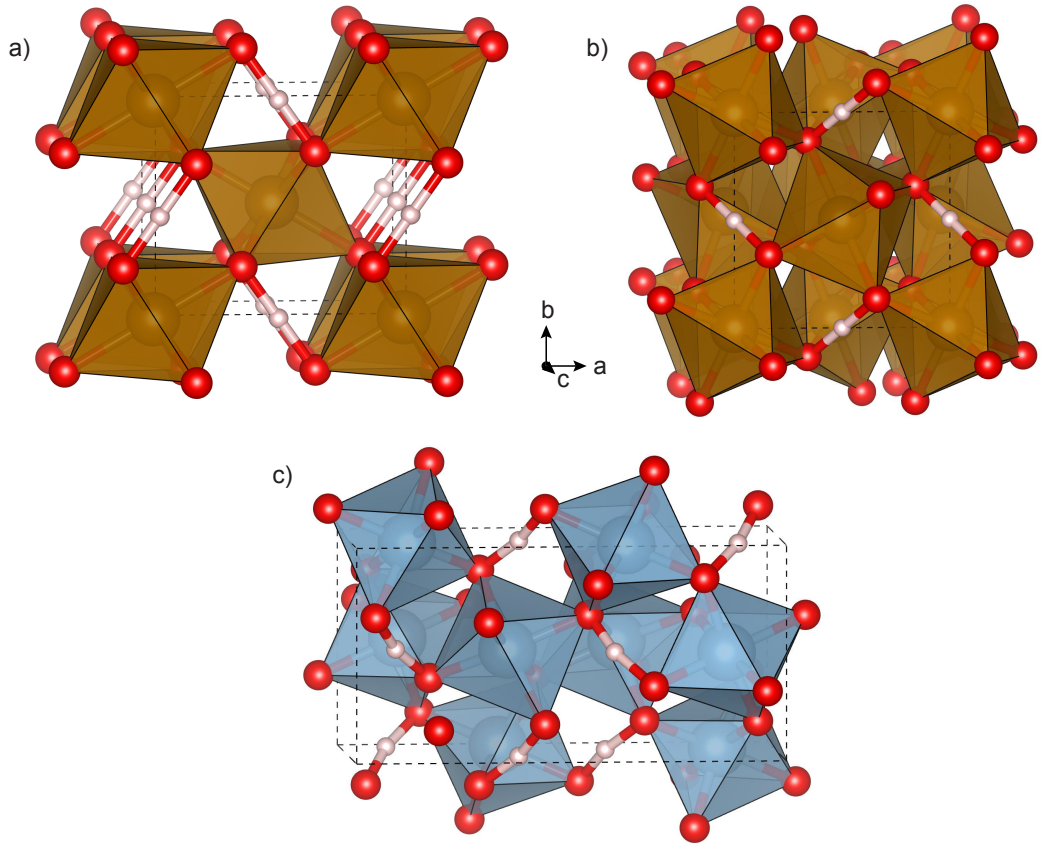

Figure 1. Polymorphs of FeO_2H and AlO_2H including (a) $CaCl_2$-type ϵ-FeOOH (Z=2), (b) cubic ($Pa\bar{3}$) pyrite-type FeO_2H (Z=4), and (c) the *Pbca* structure of AlO_2H (Z=8) reported by Verma et al. (2018). Oxygen atoms are red spheres, hydrogen atoms are white spheres, gold polyhedra are FeO_6 units, and blue polyhedra are AlO_6 units. Images were generated in VESTA (Momma & Izumi, 2008).

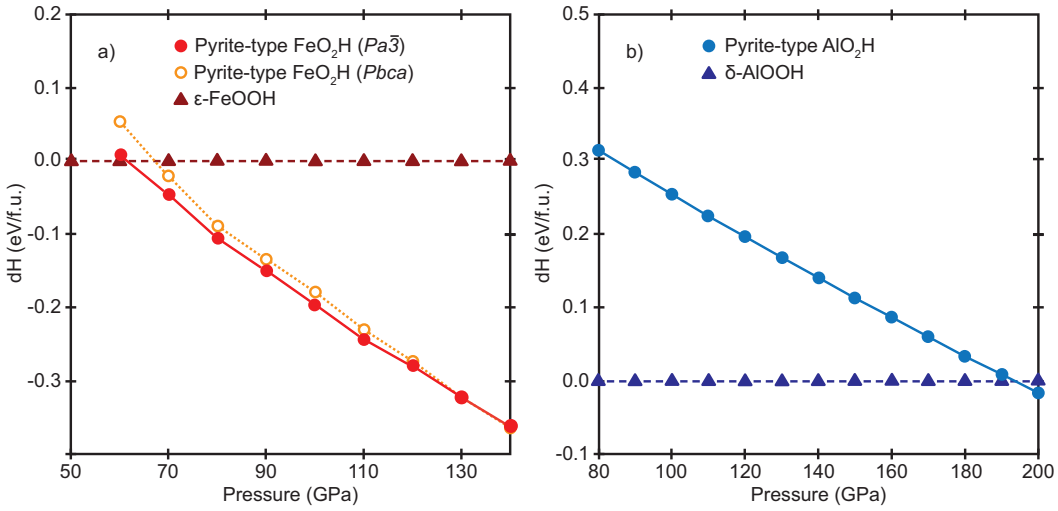

Figure 2. Calculated relative enthalpies of (a) low-spin FeO_2H and (b) AlO_2H as a function of pressure. In (a), maroon triangles indicate ferromagnetic ϵ-FeOOH, orange open circles indicate orthorhombic (*Pbca*) structure FeO_2H, and red filled circles indicate ($Pa\bar{3}$) FeO_2H. In (b), dark blue triangles indicate δ-AlOOH and light blue circles indicate ($Pa\bar{3}$) AlO_2H.

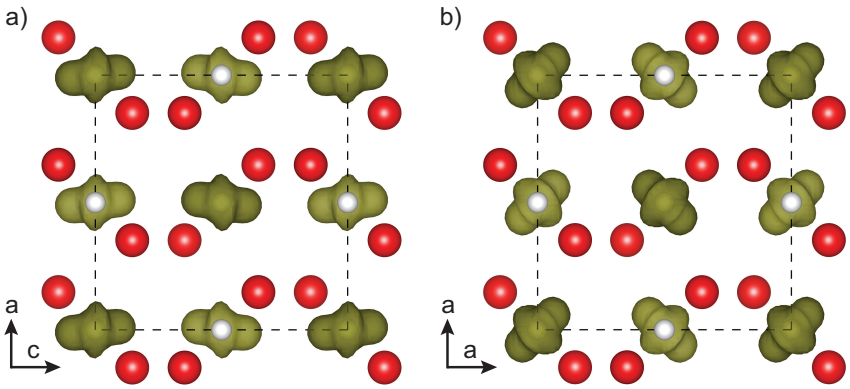

Figure 3. Spin polarization density (ρ_{up}–ρ_{down}) of (a) orthorhombic (*Pbca*) FeO_2H and (b) cubic ($Pa\bar{3}$) FeO_2H at 100 GPa. The orthorhombic distortion of the *Pbca* pyrite structure, is minor enough to be difficult to assess by eye, with b/a lattice ratios of 0.995-0.999 and b/c ratios of 1.004-1.005 in the evaluated pressure interval (60-140 GPa). Red spheres indicate oxygen atoms, white spheres indicate hydrogen atoms, and the iron atoms (shown in Figure 1) have been removed for clarity. The yellow isosurface indicates a value of 0.081 e/a.u.^{3}. Images were generated in VESTA (Momma & Izumi, 2008).

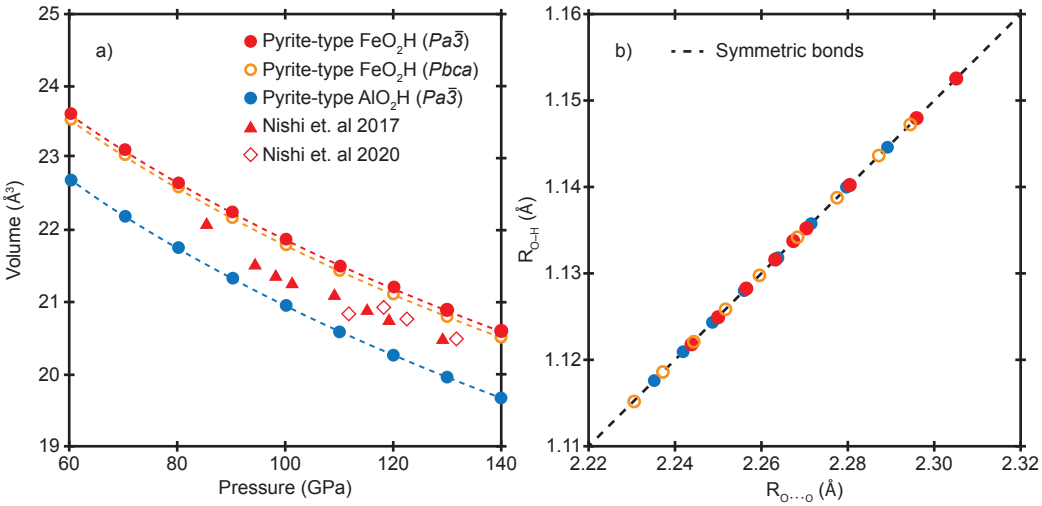

Figure 4. Computed structural parameters of pyrite-type FeO_2H and AlO_2H, including (a) volume (V/Z) with dashed lines indicating the corresponding third-order Birch-Murnaghan equations of states for each phase, and (b) hydrogen bonding as a function of pressure. Experimentally determined volumes of FeO_2H from Nishi et al. (2017) and Nishi et al. (2020) are included as filled red triangles and open red diamonds, respectively.

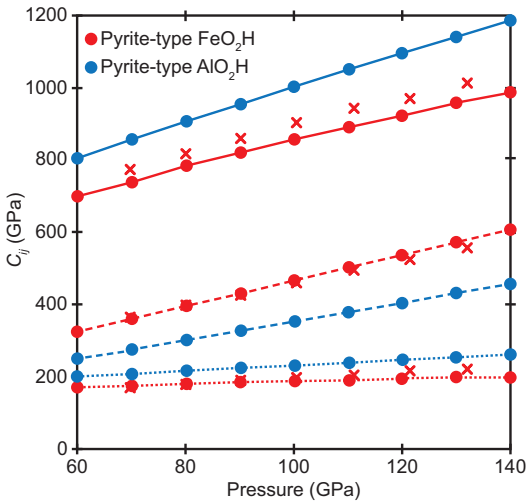

Figure 5. Elastic constants of $Pa\bar{3}$ pyrite-type FeO_2H (red) and AlO_2H (blue) as a function of pressure from 60 to 140 GPa. Solid lines indicate the C_{11} constant, dashed lines indicate the C_{12} constant, and dotted lines indicate the C_{44} constant. The FeO_2H elastic constants calculated by Huang et al. (2019) are included as red crosses.

Figure 6. (a) Sound velocities and (b) density of $Pa\bar{3}$ pyrite-type FeO_2H (red circles), pyrite-type AlO_2H (light blue circles) and lower pressure polymorphs ϵ-FeOOH (maroon triangles) and δ-AlOOH (dark blue triangles) as a function of pressure from 60 to 140 GPa compared to the Preliminary Reference Earth Model (PREM). ϵ-FeOOH and δ-AlOOH data are from Thompson et al. (2017) and Tsuchiya and Tsuchiya (2011), respectively, and the pyrite-type FeO_2H sound velocities calculated by Huang et al. (2019) are included as red crosses. All of the data result from static calculations excluding those of PREM (solid and dashed black lines) and an experimental NRIXS measurement taken at 133 GPa and room temperature by Liu et al. (2017) (red squares).

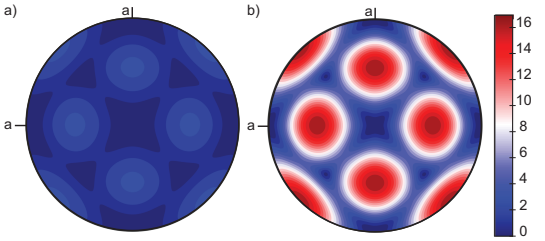

Figure 7. Lambert equal-area upper-hemisphere projections of the polarization anisotropy (AV_S) of (a) $Pa\bar{3}$ pyrite-type FeO_2H and (b) AlO_2H at 100 GPa. Figures were generated using MTEX (Mainprice et al., 2011).

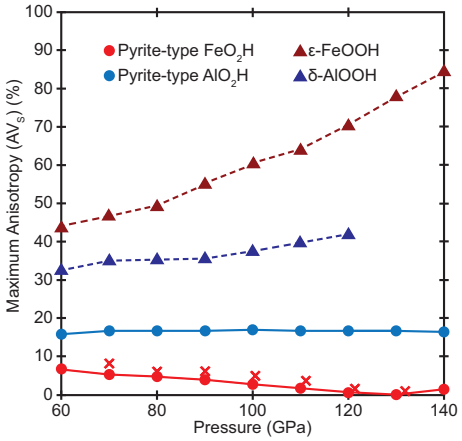

Figure 8. Comparison of the maximum anisotropy (AV_S) of pyrite-type FeO_2H (red circles) and AlO_2H] (light blue circles) to lower pressure polymorphs ϵ-FeOOH (dark blue triangles) and δ-AlOOH (maroon triangles) from 60 to 140 GPa. The ϵ-FeOOH and δ-AlOOH data are from Thompson et al. (2017) and Tsuchiya and Tsuchiya (2011), respectively. The AV_S of pyrite-type FeO_2H calculated by Huang et al. (2019) are included as red crosses.

Figure 1.

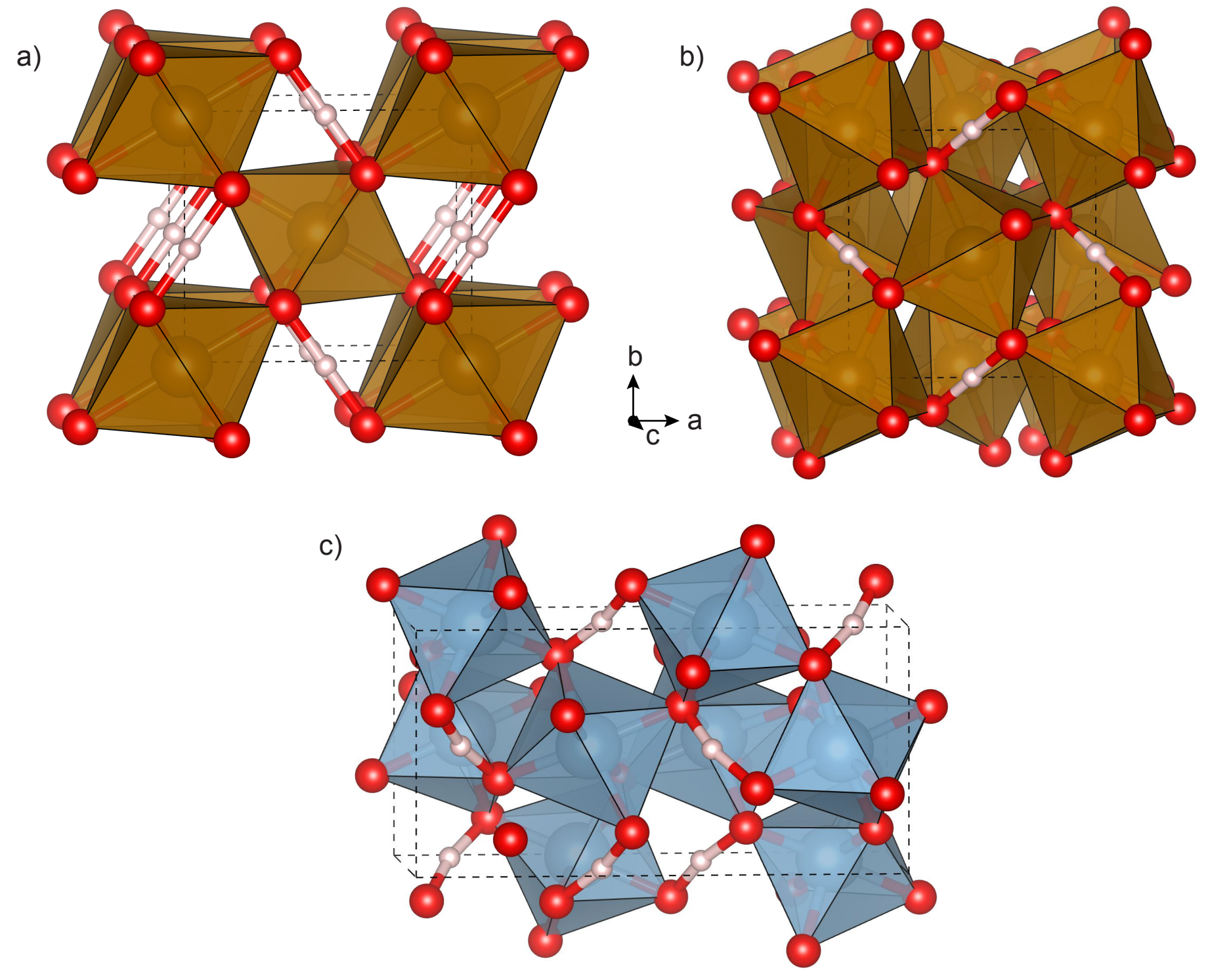
a)
b)
b
a
c
c)

Figure 2.

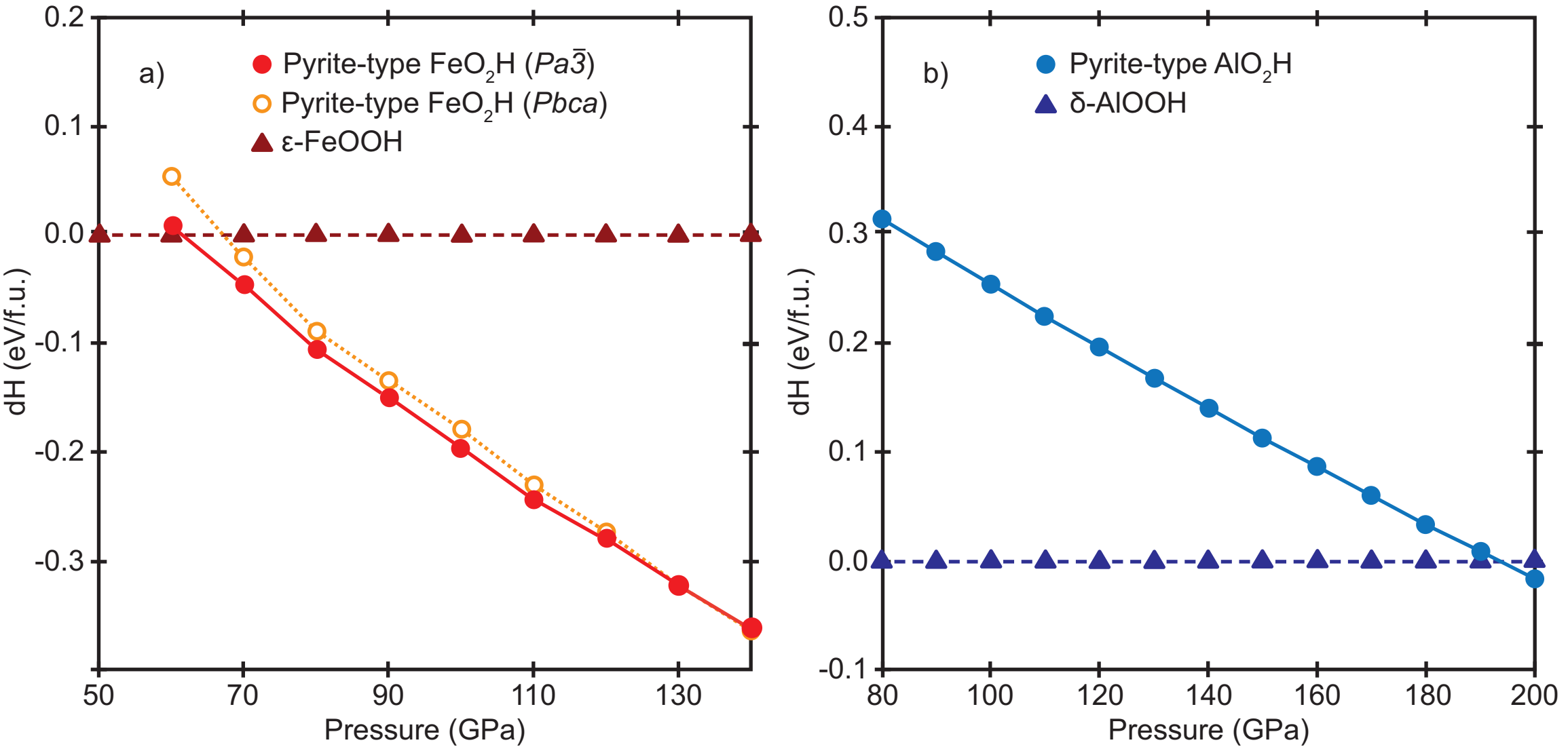
a)
Pyrite-type FeO_2H ($Pa\bar{3}$)
Pyrite-type FeO_2H (*Pbca*)
ε-FeOOH
dH (eV/f.u.)
0.2
0.1
0.0
-0.1
-0.2
-0.3
50
70
90
110
130
Pressure (GPa)
b)
Pyrite-type AlO_2H
δ-AlOOH
dH (eV/f.u.)
0.5
0.4
0.3
0.2
0.1
0.0
-0.1
80
100
120
140
160
180
200
Pressure (GPa)

Figure 3.

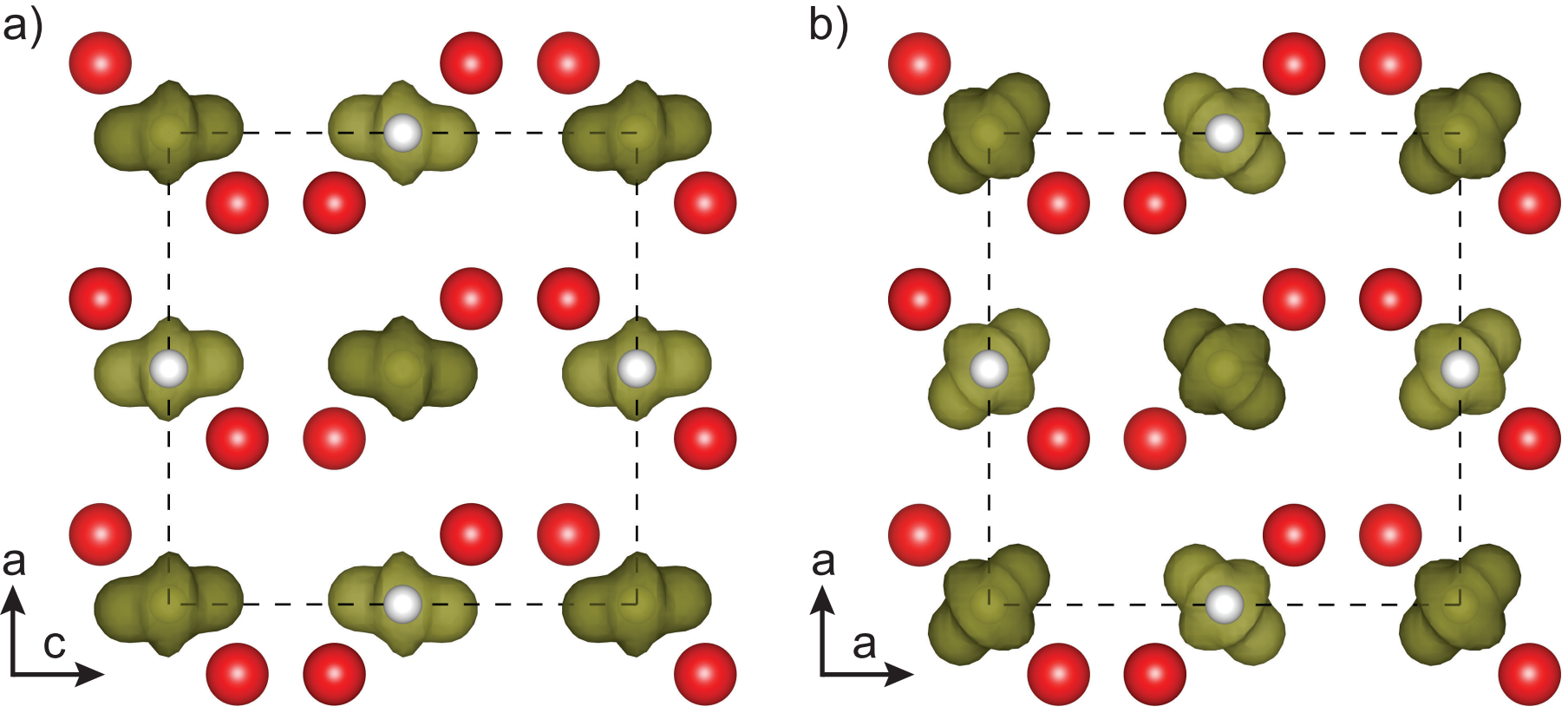
a)
a
c
b)
a
a

Figure 4.

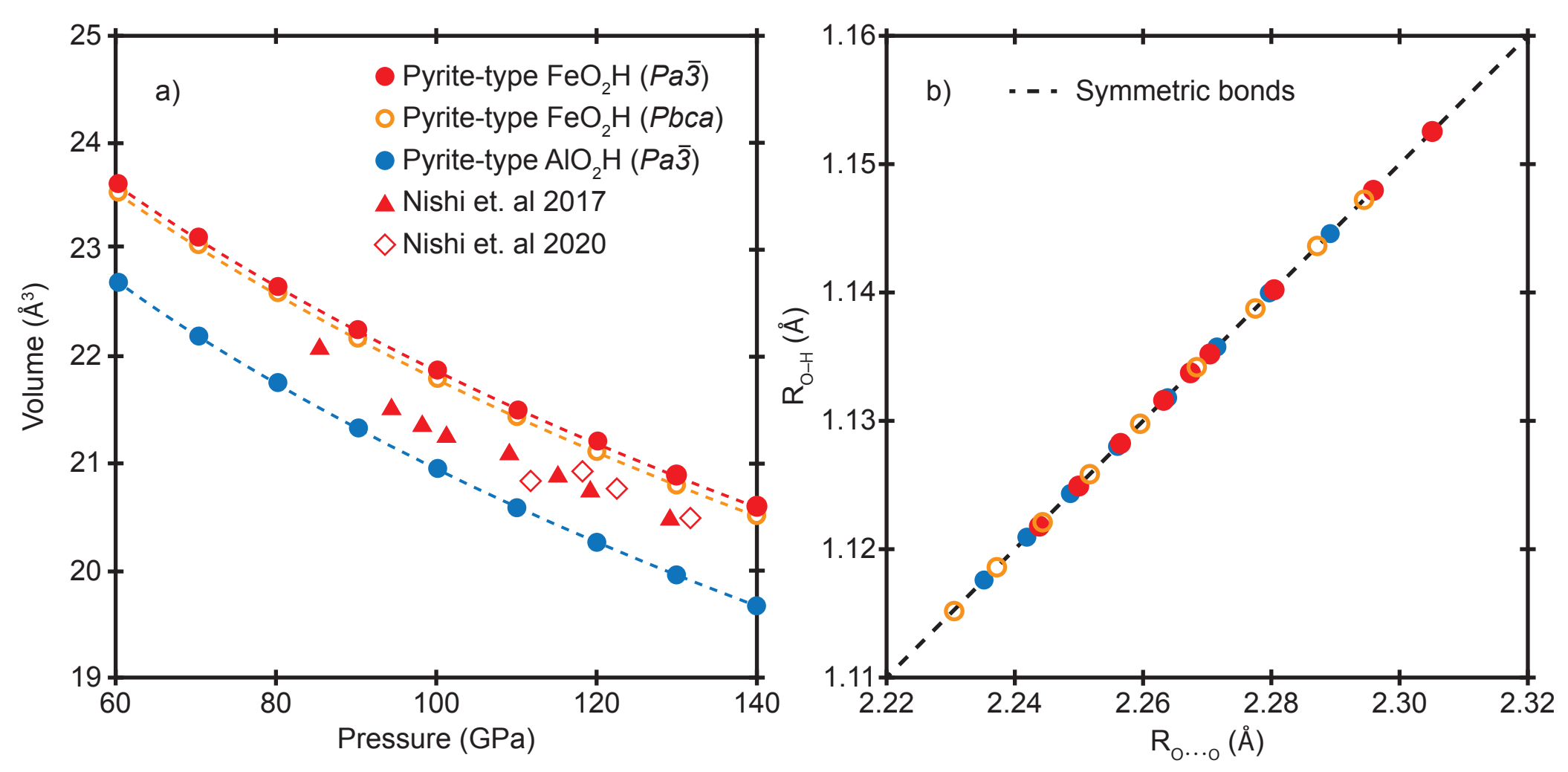
a)
Pyrite-type FeO_2H ($Pa\bar{3}$)
Pyrite-type FeO_2H ($Pbca$)
Pyrite-type AlO_2H ($Pa\bar{3}$)
Nishi et. al 2017
Nishi et. al 2020
Volume (Å^3)
Pressure (GPa)
25
24
23
22
21
20
19
60
80
100
120
140
b)
Symmetric bonds
R_{O-H} (Å)
$R_{O\cdots O}$ (Å)
1.16
1.15
1.14
1.13
1.12
1.11
2.22
2.24
2.26
2.28
2.30
2.32

Figure 5.

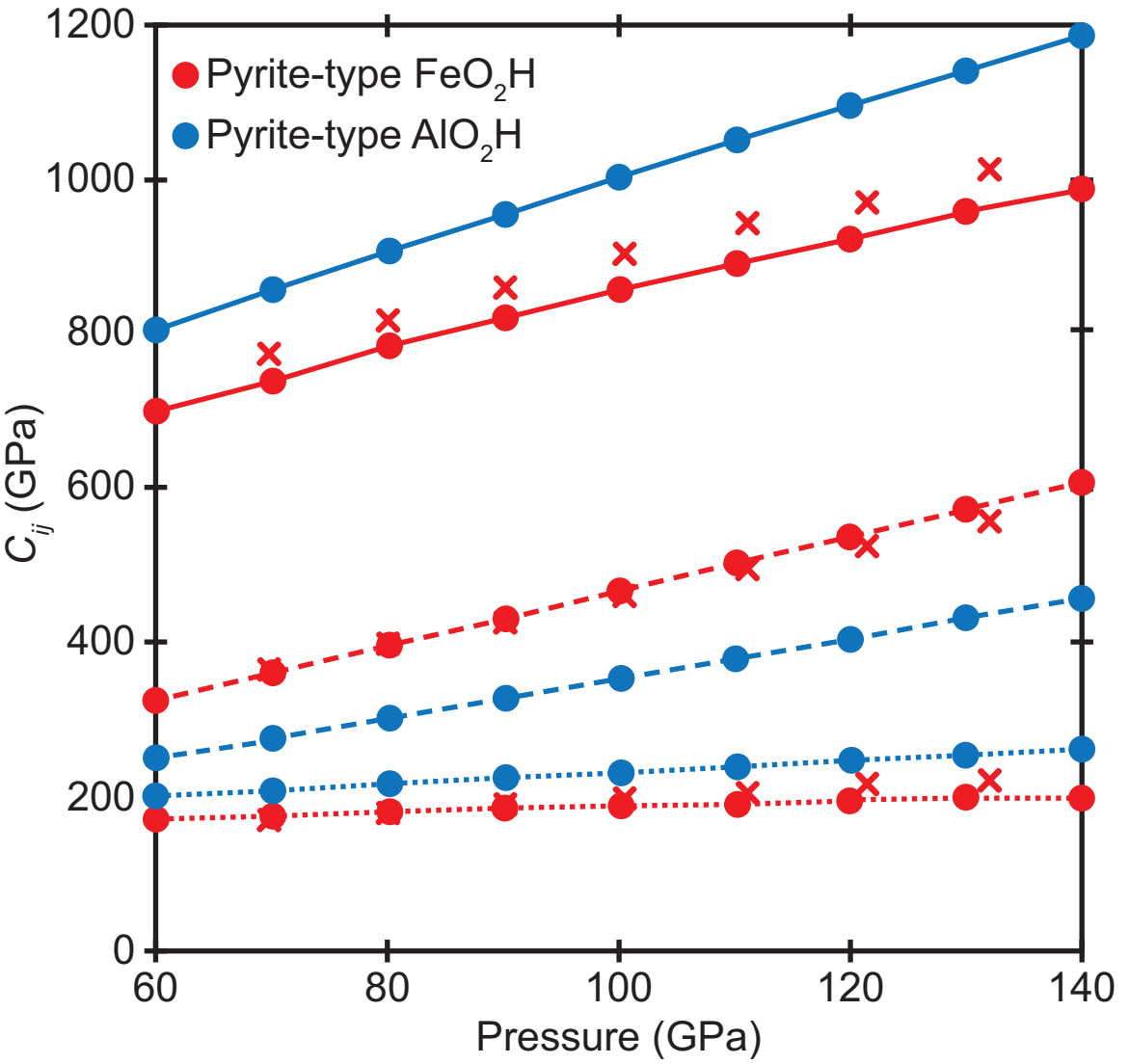
Pyrite-type FeO_2H
Pyrite-type AlO_2H
C_{ij} (GPa)
Pressure (GPa)
0
200
400
600
800
1000
1200
60
80
100
120
140

Figure 6.

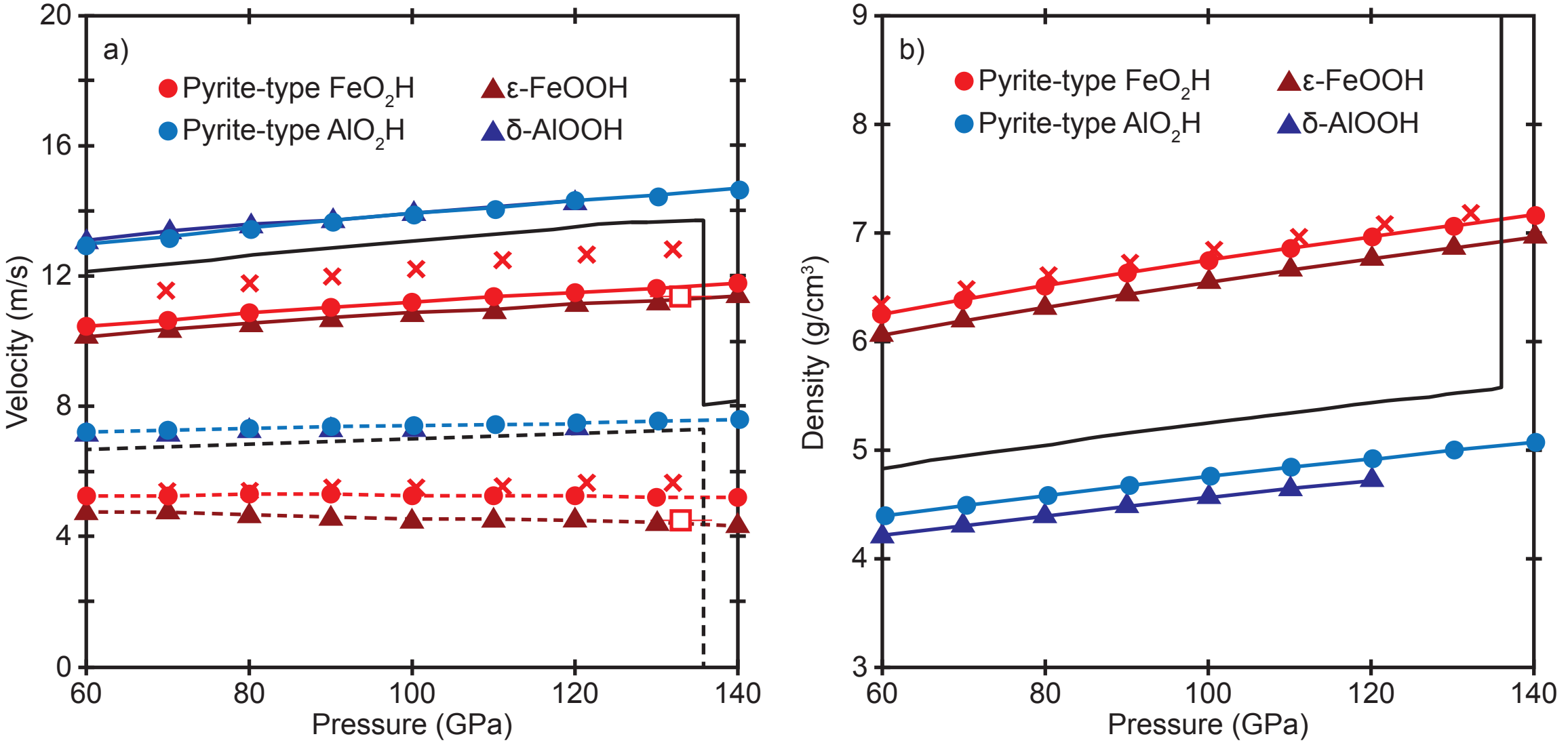
a)
Pyrite-type FeO_2H
ε-FeOOH
Pyrite-type AlO_2H
δ-AlOOH
Velocity (m/s)
Pressure (GPa)
0
4
8
12
16
20
60
80
100
120
140
b)
Pyrite-type FeO_2H
ε-FeOOH
Pyrite-type AlO_2H
δ-AlOOH
Density (g/cm^3)
Pressure (GPa)
3
4
5
6
7
8
9
60
80
100
120
140

Figure 7.

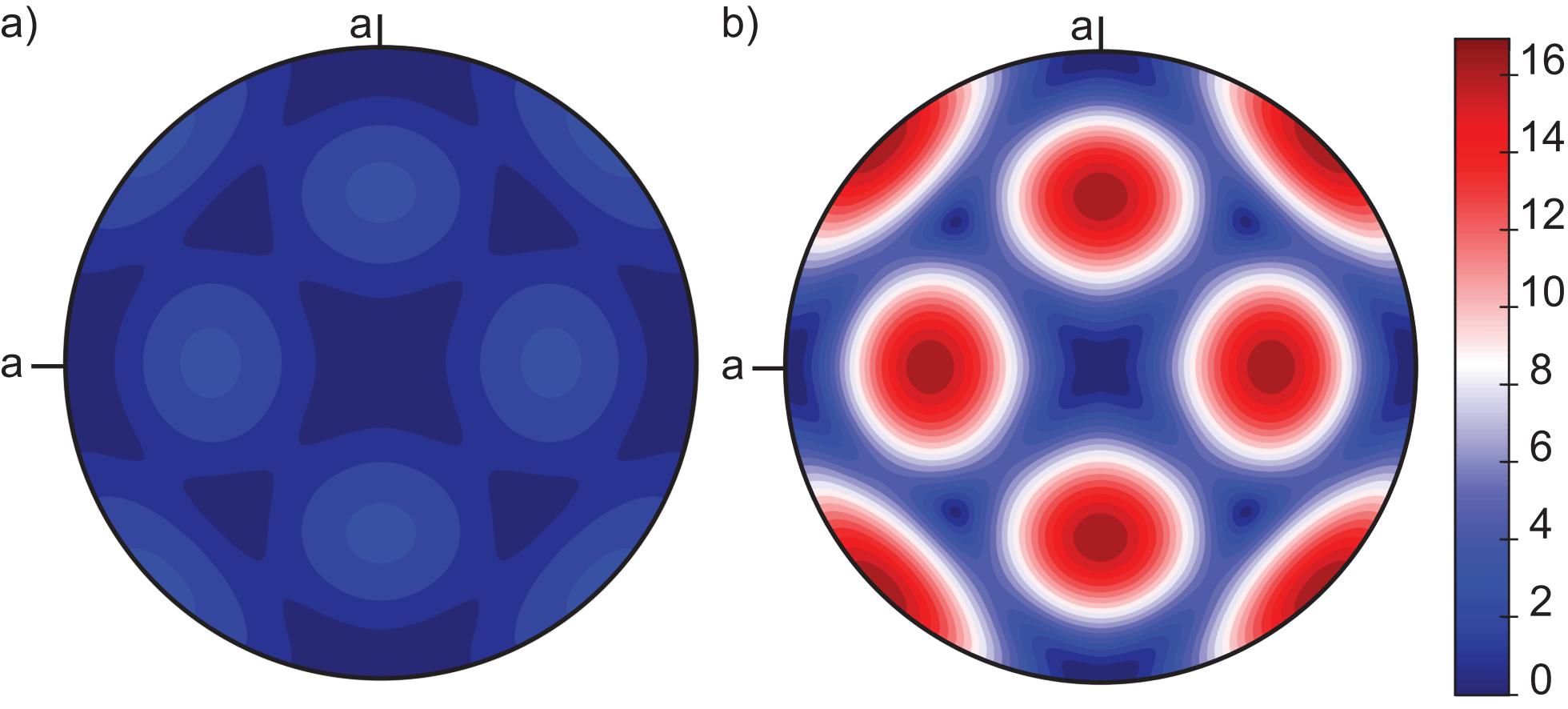
a)
a
a
b)
a
a
16
14
12
10
8
6
4
2
0

Figure 8.

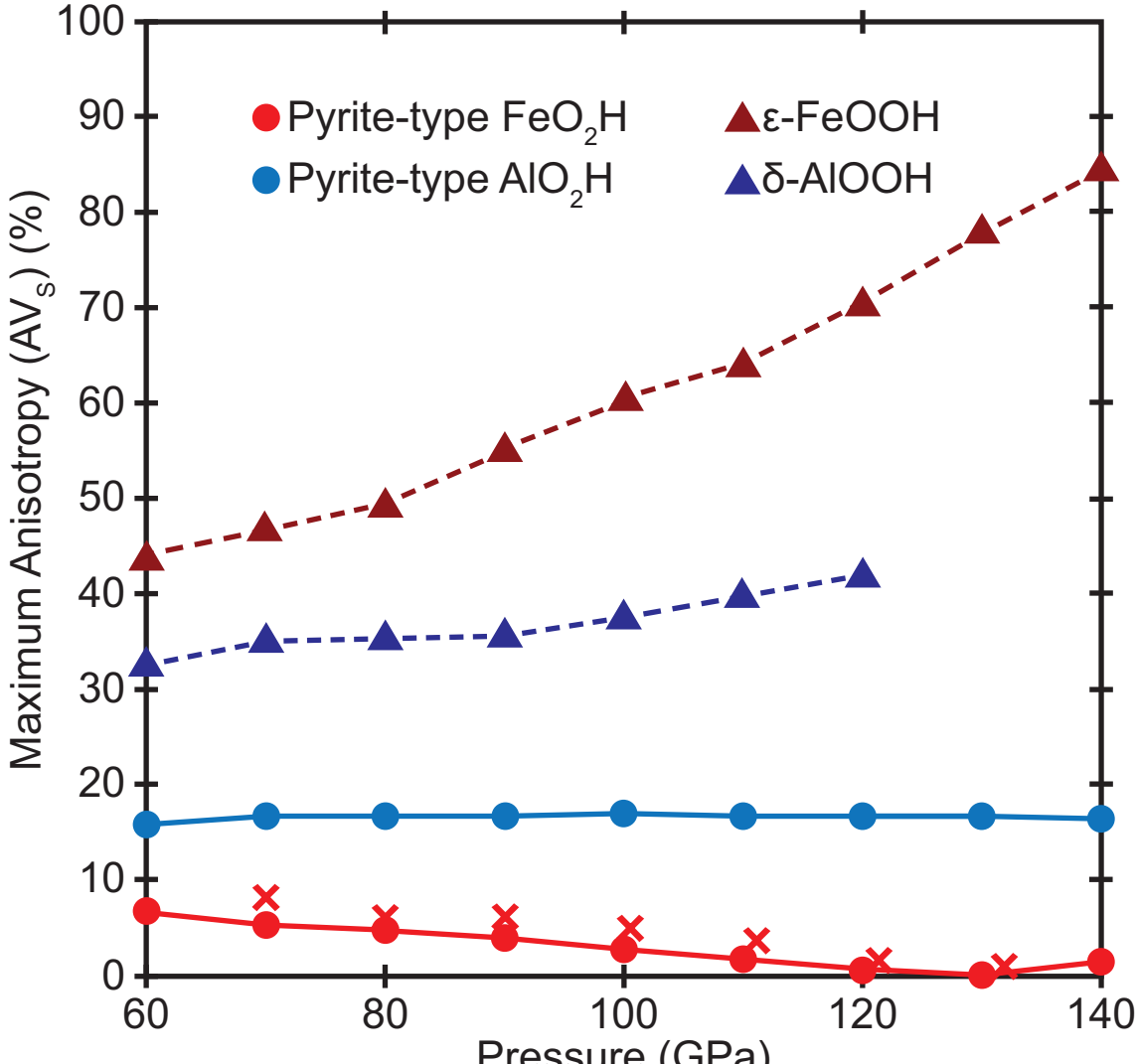
Pyrite-type FeO_2H
Pyrite-type AlO_2H
ε-FeOOH
δ-AlOOH
Maximum Anisotropy (AV_S) (%)
Pressure (GPa)
0
10
20
30
40
50
60
70
80
90
100
60
80
100
120
140